VHF imaging radar observations and theory of banded midlatitude sporadic *E* ionization layers

D. L. Hysell[1] and M. F. Larsen[2]

[1]Earth and Atmospheric Sciences, Cornell University, Ithaca, NY, USA

[2]Physics and Astronomy, Clemson University, Clemson, SC, USA

Key Points.

1. Quasiperiodic (QP) sporadic *E* layers observed under the midlatitude trough using coherent scatter radar. 2. Radar imagery shows secondary bands of irregularities normal to the primary QP bands. 3. The secondary bands are attributed to secondary Kelvin Helmholtz instability in the lower thermosphere

Abstract.

Observations of backscatter from field-aligned plasma density irregularities in sporadic *E* (E_s) layers made with a 30-MHz coherent scatter radar imager in Ithaca, New York are presented and analysed. The volume probed by the radar lies at approximately 54° geomagnetic latitude, under the midlatitude trough and at the extreme northern edge of the zone where E_s layers are prevalent. Nonetheless, the irregularities exhibit many of the characteristics of quasiperiodic echoes observed commonly at lower middle latitudes. These include a tendancy to occur in elongated bands stretching from northwest to southeast in the northern hemisphere separated by tens of kilometers and propagating to the southwest. In addition, the irregularities were found to exhibit finer-scale structures with secondary bands oriented nearly normally to the primary bands. We investigate the proposition that the primary bands are telltale of E_s-layer structuring caused by neutral Kelvin Helmholtz (KH) instability in the lower thermosphere and that the secondary bands signify secondary KH instability. Results from a 3D numerical simulation of KH support this proposition.

Introduction

The altitude range in the mesosphere/lower thermosphere where the turbopause occurs, i.e., near an altitude of 100 km, is particularly important because of the rapid changes in dynamics, electrodynamics, and chemistry that occur there. The transition from the negative lapse rates in the mesosphere to isothermal and even positive lapse rates in the lower thermosphere is a natural inhibitor to significant vertical transport across that region due to the inherently more stable air overlying the less stable air in the mesosphere. Layers in the mesosphere frequently show evidence of shear instabilities of the Kelvin-Helmholtz type, as shown in the case studies presented by *Hecht et al.* [2021] and *Chau et al.* [2020], for example. See also their discussion of other past observations from that region.

Observations from higher altitudes near the critical turbopause transition are much more limited, but the available data indicate that the region is characterized by frequent and persistent shears associated with the large winds that occur there. The shears often meet the criteria for shear instability, as shown by *Larsen* [2002] using an extensive set of rocket-based wind measurements and by *Sherman and She* [2006] using a long time series of lidar wind measurements that extended to altitudes of 105 km. *Liu* [2017] was able to reproduce the essential characteristics of the observed winds and shears in that altitude range and discussed their implications for diffusion and transport. Recently *Mesquita et al.* [2020] presented an example of a K-H billow observed directly with chemical tracer measurements in the transition altitude where the more stable isothermal lapse rate occurs. One conclusion was that this type of instability can contribute significantly to vertical transport into the more stable portions of the atmosphere in the lower thermosphere, which would otherwise inhibit strong vertical motions.

Data from the lower thermosphere are much more limited than data from lower altitudes in the mesosphere, but a long series of observations from the Caribbean have shown that there is a strong relationship between the development of coherent scatter radar echoes associated with sporadic E layers and upward displacements of the ionization layers. Furthermore, the quasi-periodic (QP) scattering structures that are now known to be a common characteristic of SpE layers have been tied to unstable shears in many of the observations. The vertical displacements associated with the billow structures are therefore the likely driver for the plasma instabilities responsible for the quasi-periodic structure in the radar scatter.

The sporadic E coherent scatter has a much stronger seasonal dependence than the occurrence of the strong shear layers as shown by the statistical analyses of *Larsen* [2002] and *Sherman and She* [2006] cited above. A strong shear is therefore not sufficient to produce the scattering layers, but the layers can provide another source of data related to the characteristics of the shear instabilities in that altitude range when the layers are present.

We report here on observations of coherent scatter from plasma density irregularities in sporadic *E* (E_s) layers over the Great Lakes region of North America made with 30 MHz radar imager located in Ithaca, New York. The E_s-layer echoes have the characteristics of the so-called quasiperiodic (QP) echoes made famous in a series of studies conducted at the 50-MHz MU radar in Japan (e.g. *Yamamoto et al.* [1991, 1992, 1994]). In range-time-intensity format, the echoes appear as multiple, narrow, parallel striations. The echoes are not truly periodic, but the multiplicity of slanted striations sometimes gives them a quasiperiodic character depending on their range rate or slope. The echoes typically appear in clusters, with episodes lasting for about 30–60 min. QP echoes and related E_s-layer ionospheric irregularities have been observed with coherent scatter radars in numerous midlatitude locations as described, for example, by

Ecklund et al. [1981]; *Riggin et al.* [1986]; *Bourdillon et al.* [1995]; *Haldoupis et al.* [1996]; *Chu and Wang* [1997]; *Tsunoda et al.* [1998]; *Chau and Woodman* [1999]; *Hysell and Burcham* [2000]; *Rao et al.* [2008].

Background

The echoes discussed in this paper are most directly comparable to those observed by a coherent scatter radar deployed on St. Croix in a campaign in 2002 and then continuously between 2008–2018 – see for example *Larsen et al.* [2007]; *Hysell et al.* [2004, 2009, 2010, 2012]. The St. Croix radar was functionally similar to the Ithaca radar and also had its main beam directed to the northwest which affects the presentation of the echoes in RTDI format. The St. Croix radar used imaging techniques to resolve certain spatio-temporal ambiguities otherwise in the data and to yield a plan view of the E_s-layer irregularities. The St. Croix studies moreover benefited from close proximity to the Arecibo Radio Observatory where plasma and neutral state parameters could be measured in a common volume. Here, we summarize the salient findings of the St. Croix/ Arecibo experiments.

1. QP echoes arise from bands of E-region ionization tens or hundreds of km long, separated typically by about 30 km, and propagating to the southeast at about 50 m/s while maintaining approximately constant altitude. The streaks in coherent scatter range-time-Doppler-intensity (RTDI) plots reflect the proper line-of-sight motion of the bands and discrete features within them. The ionization bands were observed routinely using Arecibo incoherent scatter modes and, on one occasion, in 557.7 nm airglow imagery [*Hysell et al.*, 2012].

2. Fine structure in the Doppler shifts of the coherent scatter are indicative of $E \times B$ electron drifts and the underlying polarization electric field arising in regions where the background conductivity is inhomogeneous. In one study, variations in the Doppler shift were shown to

be highly correlated with variations in E_s layer height, i.e., with variations in the local Hall conductivity [*Hysell et al.*, 2010]. When the electron drift speed exceeds the ion-acoustic speed, so-called type I echoes indicative of Farley Buneman waves result.

3. The ionization bands are embedded in neutral flows exhibiting strong vertical shear. Not only is the shear thought to create the E_s layers, it has been found to be Kelvin-Helmholtz unstable in the Richardson number sense, implying that it can also create the bands. Unmistakable Kelvin-Helmholtz cats eyes have been observed in an irregular E_s layer over Arecibo. The motion of the ionization bands has furthermore been found to be consistent with the neutral wind velocity at the shear node in unstable MLT wind profiles measured over Arecibo [*Hysell et al.*, 2012].

4. One or more gradient drift-type plasma instabilities are thought to be responsible for generating additional structuring in E_s layers and ultimately for producing the field-aligned irregularities detected by coherent scatter radars (e.g. *Seyler et al.* [2004]). A drift wave-type instability was shown to be able to produce kilometric plasma density irregularities starting from the larger banded irregularities seen in ISR data [*Hysell et al.*, 2013].

A distinguishing feature of the Ithaca radar is its high magnetic latitude. The *E*-region volume from where field-aligned backscatter is expected lies to the east of Lake Huron at latitudes between 44.5–45.5°N or between 53.65–54.65° geomagnetic. This is higher than even the Valensole radar in the south of France located at 43.8° geographic and just 37.1° geomagnetic [*Haldoupis et al.*, 2001]. The region furthermore falls under the midlatitude trough where *F*-region densities have a minimum (e.g. *Yang et al.* [2015]). *Yu et al.* [2019] mapped the global climatology of E_s layers using GPS radio occultation measurements from the COSMIC satellites, finding a steep decline in intensity above about 50° geomagnetic latitude. The authors attributed this to the failure of the wind shear mechanism for creating E_s layers at higher dip latitudes. However, recent observations of QP echoes made during ionospheric modification experiments at the HAARP facility suggest that at least some of the processes at work at lower latitudes also take place in the subauroral *E* region [*Hysell et al.*, 2018b]. One of the objectives of the present research is to explore the latitude extent of midlatitude E_s-layer formation and instability.

The central question in QP-echo research, however, is the mechanism responsible for producing large-scale irregularities and bands in E_s layers in the first place. Neutral wind shear is an obvious source of free energy and so is suspected to play a key role. A plasma instability similar in some respects to the one proposed by *Perkins* [1973] except in the *E* region was suggested by *Cosgrove and Tsunoda* [2002]. The background forcing in that case is provided by vertical wind shear in the MLT region. The winds drive currents with opposing directions in the crests and troughs of a wavelike perturbation. The resulting polarization electric fields cause electron convection that intensifies the initial layer perturbation (while the ions follow suit to preserve quasineutrality). As with Perkins' instability, the E_s layer instability prefers waves that propagate at oblique directions with respect to cardinal magnetic coordinates. The instability can be robust since conductivity gradients in patchy E_s layers can be exceptionally steep. The fastest-growing waves are expected to have a wavelength of a few to a few tens of km [*Cosgrove*, 2007].

Larsen [2000] proposed instead that the vertical wind shears were unstable in the Richardson-number sense to Kelvin Helmholtz instability. In this theory, the ionization bands underlying the QP echoes represent plasma drawn from E_s layers and entrained in the Kelvin Helmholtz billows. Evidence for the theory came from wind profile measurements made with chemical releases from sounding rockets demonstrating that the instability criterion could be met in the midlatitude MLT as well as from Arecibo ISR observations seemingly demonstrating the entrainment process in action [*Miller and Smith*, 1978]. Numerical simulations in two dimensions lent additional support to the theory [*Bernhardt*, 2002]. The aforementioned studies from St. Croix and Arecibo, providing incisive observations of the bands in profile and plan view together with vector neutral wind profile estimates. In the studies, the dispersion characteristics for Kelvin Helmholtz waves matched the observations.

Below, we test the *Larsen* [2000] theory further. In particular, theory predicts secondary waves associated with neutral Kelvin Helmholtz instabilities. Imaging data from the Ithaca radar offer a means of testing this theory while also investigating QP-echo behavior at latitudes near the midlatitude trough.

Observations

We report here on observations of coherent scatter from plasma density irregularities in sporadic E (E_s) layers made with a 30 MHz radar imager locate near Ithaca, New York (42.444° N, 283.498° E, 51.64° geomagnetic). The radar is similar to the one deployed on St. Croix, USVI, over the past two decades – see *Hysell et al.* [2018a] and references therein for description. It employs arbitrary waveform synthesis for transmission and software-defined receivers for reception. Transmission is performed using an array of eight five-element Yagi antennas with a gain of approximately 20 dBi and a main beam directed at 330° azimuth angle. The expected range to E region scatterers is between about 850–1100 km.

The nominal transmit waveform is a 28-bit maximal length binary phase coded pulse with a baud width of 10μs. The nominal pulse repetition frequency (PRF) is 250 Hz, implying an interpulse period (IPP) of 4 ms (600 km) and a duty cycle of 7%. Doppler shifts between ±625 m/s can be unambiguously resolved using this PRF. The peak transmitter power is 8 kW.

Reception uses six groups of Yagi antennas composing 15 nonredundant interferometry baselines, the longest of which being approximately 15 wavelengths long. For the data shown below, processing involved computing spectra and cross-spectra from 24-point samples and incoherently integrating the results in groups of 31, yielding an overall experimental cadence of one every three seconds. Imaging is performed using aperture-synthesis methods (see below).

The radar is deployed sufficiently close to the Millstone Hill Observatory to permit common-volume coherent and incoherent scatter observations. Simultaneous observations were not undertaken for the experiments described here but are planned for the future. An ionosonde located in Alpena, Mi. (45.1°N, 276.4°E, 54.1°N geomagnetic) ran throughout the operations of the Cornell radar, however, and sporadic *E* layers in the Alpena ionograms proved to be reliable indicators of coherent scatter from the volume probed by the radar. See *Reinisch and Galkin* [2011] for a description of the ionosonde.

The radar became operational in mid July, 2020, toward the end of sporadic *E* season. Coherent scatter from sporadic *E* layers was observed shortly after sunset on the nights of July 16, July 19, August 5, and August 11 (UT dates). The F10.7 solar flux index increased almost linearly from 71 to 76 during this interval which was geomagnetically quiet.

Fig. 1 shows backscatter received by the radar on July 16, August 5, and August 11, 2020 (UT dates) in range-time-Doppler-intensity format. Here, UT = EST + 5 = EDT + 4. The ordinate of each panel is the apparent range to the target. This is the true range for echoes from aircraft seen at short ranges as well as for specular and non-specular meteor echoes which predominate below about 300 km. Note that August 11, 2020, was near the peak of the Perseid meteor shower, explaining the high incidence of strong meteor echoes.

The values of FoEs measured by the ionosonde in Alpena are shown in the panel in the lower-right corner of the figure (see `http://https://hpde.io/SMWG/Observatory/GIRO`). Sporadic *E* layers were obviously present over Alpena at the dates and times in question, although peak E_s-layer densities do not correspond closely to the times when the most intense echoes were being received by the radar. Experience from the Caribbean showed that strong coherent scatter generally occurs when the difference between FoEs and the blanketing frequency is large, i.e., when the E_s layer is patchy.

Echoes from E_s layer irregularities are range aliased in these observations, their true range equal to their apparent range plus the IPP. The IPP was changed from 750 km on July 16 to 600 km thereafter due to interference that was pulsed and synchronous with the former IPP. This interference is evident in the RTDI panel for July 16, 2020 **where it appears as stray vertical bands at all ranges simultaneously. This should not be confused with the meteor echoes which are sometimes strong enough to have visible range sidelobes.**

The brightness, hue, and saturation of the pixels reflect the signal-to-noise ratio, Doppler shift, and spectral width according to the legends shown. Signal-to-noise ratios exceeded 20 dB at times. The range rates of the echoes were both positive and negative at times and approximately matched their Doppler shifts which were limited to about $\pm$ 60 m/s. Large Doppler shifts indicative of type I echoes and Farley Buneman waves of the kind described by *Schlegel and Haldoupis* [1994] were not seen in these preliminary data.

Aperture synthesis images of the coherent backscatter can be formed from all the pairwise interferometry measurements afforded by the spaced-receiver data collected in Ithaca. Six spaced receiver groups imply fifteen nonredundant interferometry baselines. Interferometry is performed in the frequency domain, and images for each Doppler frequency are then combined to form composites. One image is available every 3 s here, and animating the images reveals the dynamics behind the RTDI images. The imaging methodology used here was described by *Hysell and Chau* [2006].

Fig. 2 shows images representative of the backscatter shown in the RTDI plots. The dashed contours in the images give the altitude where the condition for field-aligned backscatter is exactly met assuming straight-line propagation. The contours actually give only rough altitude estimates as the 30 MHz rays can undergo significant bending as they penetrate the E_s-layer irregularities in question [*Hysell et al.*, 2002].

The images show that the backscatter arrived from bands separated by about 20–40 km, extending from northwest to southeast and propagating to the southwest. The propagation speed is about 60 m/s, giving a period of 5–10 min. There are persistent bright spots in the bands, and these give rise to the closely-spaced streaks evident in the RTDI plots. These findings are all consistent with prior results from St. Croix and elsewhere. Since the radar beam is directed to the northwest from Ithaca, echoes from bands propagating to the southwest should and do exhibit modest range rates which can be positive or negative. (Note that the MU radar most often observes E_s-layer irregularities looking northward so that bands propagating to the southwest predominantly result in echoes with negative range rates.) The lifetimes of the bands are less than 30 min. which is shorter than the time it would take them to traverse the radar-illuminated volume.

The most novel and remarkable features of the Ithaca observations are depicted in Fig. 3. The figures represent intervals when the scattering bands exhibited significantly horizontal broadening. The broadening possibly reflects the emergence of secondary bands oriented nearly normally to the original, primary band or bands. The secondary bands are not quite normal to the primaries but appear to be tilted or threaded like a screw. This is particularly obvious in the images from August 11, 2020, where eight oblique secondary bands can be seen. The distance between adjacent secondary bands is approximately 10 km. These features are the focus of this paper and the subject of the discussion to follow.

The Ithaca observations differ from the St. Croix observations in a number of respects. For example, the range to the targets is approximately three times larger for the former than the latter. As the scatterers are not beam filling, we might expect the received signal intensity to scale with range as r^{-4}, implying a $\sim$20 dB relative deficit in intensity for the former. That the strongest signals received from Ithaca so far are within 10–13 dB of the strongest echoes ever received from St. Croix suggests that the instabilities at work over the Great Lakes are, in some respects, **more** intense as those over the Caribbean.

Conversely, the QP echo events reported here were few in number and short in duration compared to what has typically been seen from St. Croix and at the MU radar. The Doppler shifts were also confined to small values, well below the threshold for Farley Buneman instability in particular, whereas Farley Buneman waves are fairly common features of radar observations from St. Croix. The Ithaca dataset is **not** yet very extensive, and we do not know whether QP echoes are typically less robust at the dip latitudes in question here than at lower middle latitudes.

Most importantly for this paper, we have two examples of secondary striations in the initial Ithaca radar dataset. While examples of this phenomenon can be found in the St. Croix data (see for example *Hysell et al.* [2012]), the examples presented here are by far the clearest. We consequently turn our attention to a possible explanation for this phenomenon.

Theory and analysis

Secondary instabilities in stratified media are important in any number of geophysical contexts because they represent an intermediate state between laminar and turbulent flow and can significantly affect transport and dissipation (see *Thorpe* [2012] for review.) Secondary instability in two-dimensional sheared flows were recognized first by *Corcos and Sherman* [1976] who identified instability on the thin braids between billows where the shears are the strongest. Billow pairing or 'amalgamation instability' was also found to occur in two dimensions. The first secondary instability in three dimensions was modeled by *Klaassen and Peltier* [1985], a convective instability in the overturning billows. Three-dimensional structuring was also shown to accompany billow pairing [*Smyth*, 1999].

Subsequently, four types of three-dimensional instabilities were identified using numerical simulations [*Martinez et al.*, 2006]. Two of these occur on the braids, and the other two occur near or within the billow cores. *Mashayek and Peltier* [2012] determined the parameter spaces (in terms of the Richardson, Reynolds, and Prandtl numbers) where instabilities occur, finding generally that large Reynolds numbers, small Richardson numbers, and intermediate Prandtl numbers are most conducive to growth. *Thorpe* [1987] identified two additional 3D instabilities on the basis of laboratory experiments. These include knot instabilities, which occur when billows intersect, and tubes, which connect billows together.

Fritts et al. [2021] carried out a series of state-of-the-art numerical simulations of K-H instability structures for conditions appropriate to the less stable mesosphere region with the goal of explaining some of the featurs observed by *Hecht et al.* [2021] in their ground-based imager data. Structures in their simulations are reminiscent of the structures observed in the radar scatter. In particular, the radar images for all three days presented here show the banded structure associated with secondary instabilities in the *Fritts et al.* [2021] simulations. The radar image for August 11 in Figure 2 also shows a structure similar to the new tube formation in Figure 9 of the latter paper. The radar image for later in the same night (Figure 3) shows evidence of structure similar to the twist waves in Figure 9 of that paper.

To further investigate secondary instabilities in the MLT region, we consider a simple numerical simulation of dynamical instability in three dimensions with parameters that directly match the conditions in the altitude range of the sporadic E layers. We consider incompressible motion in the Boussinesq limit, neglect thermodynamic effects, and impose the conversation of neutral momentum and mass density:

$$\frac{\partial \mathbf{u}}{\partial t} = -\nabla P - R_i \rho \hat{z} + \frac{1}{R_e}\nabla^2 \mathbf{u} \tag{1}$$

$$\nabla \cdot \mathbf{u} = 0 \tag{2}$$

$$\frac{\partial \rho}{\partial t} + \mathbf{u}\cdot\nabla\rho = \frac{1}{R_e S_c}\nabla^2 \rho \tag{3}$$

where $\mathbf{u}(x,y,z)$ is the velocity, $\rho(x,y,z)$ is the perturbed mass density, and $P(x,y,z)$ is the generalized pressure. We regard ρ as a perturbation to the background mass density which is in hydrostatic balance, the underlying force balance having already been removed from Eq. 1. The perturbed density will also serve as a tracer in this problem.

The model is stated in terms of three dimensionless parameters: the Reynolds number $R_e \equiv UL/\nu$, Richardson number $R_i \equiv N^2/U'^2$, and Schmidt number $S_c \equiv \nu/D$. Here, ν is the kinematic viscosity, U is the flow differential across the shear layer, U' the maximum gradient of U, L the depth of the shear layer, N the Brunt Vaisala frequency, and D is the diffusivity.

The simulation encloses a volume in rectangular coordinates two unit lengths wide in both horizontal dimensions $L_x = 2, L_y = 2$ and one unit length wide in the vertical $L_z = 1$. The initial conditions are:

$$u = F \tanh(z/a) \quad (4)$$

$$w = A \sin(4\pi x/L_x) \exp(-z^2/\sigma^2) \quad (5)$$

$$\rho = \exp(-(z/4a)^2) \quad (6)$$

where z is measured from the vertical center of the volume and with F = 0.5, A = -0.2, a = 0.05, and σ = 0.2 here. Adopting a characteristic length scale of 30 km and a timescale of 300 s implies a simulation 60 km × 60 km × 30 km in size, wind speeds $u \in \pm 50$ m/s, and a vertical shear length scale of 1.5 km **which is a in dimensional units**. The quantity v is initialized with Gaussian noise at the level of 5.0×10^{-3}.

Neglecting buoyancy and boundary effects, the fastest-growing eigenmode is expected to have a wavelength given by $\lambda_x \gtrapprox 4\pi a \sim 0.65$ in non-dimensional units in this case [*Hazel*, 1972]. We initialize the simulation here with a vertical velocity (w) perturbation intended to seed billows with a horizontal wavelength of unity, close roughly to the size of the most unstable normal mode.

Initial boundary value simulations of the system were conducted using the Dedalus numerical package [*Burns et al.*, 2020]. The gridding for the problem is spectral, employing a Fourier basis in the horizontal directions and a Chebychev basis in the vertical in this case. The package uses a tau method for discretization to enforce generalized boundary conditions and to produce sparse banded matrices for efficient computation. Time integration is performed with mixed implicit-explicit multistep integrators with timesteps set by the **Courant-Friedrichs-Lewy (CFL) condition that the displacement of a fluid parcel during a time step must be**

smaller than the grid size. The number of grid points in the streamwise, spanwise, and vertical directions are 94, 48, and 128, respectively.

Fig. 4 shows results for nondimensional simulation time $T = 10$ following the formation of a pair of billows and the onset of secondary instability. In dimensional time, the figure depicts 50 min. of instability evolution. By this time, secondary instability is seen to have created structure in the billow cores as well as in the intervening braids. Of most significance for the present problem is the production of secondary irregularities in the spanwise direction, mainly at the core boundaries. Their location and morphology of the irregularities indicates that they are convective in nature. The irregularities appear as protrusions from the billow cores that alternate from one side to the other in a plan view. Six protrusions can be seen on either side of the cores, implying that the secondary instabilities have a primary wavenumber three times that of the main instability. In dimensional units, the secondary instabilities have a wavelength of about 10 km.

Additional insight comes from viewing the simulation results in three dimensions as shown in Fig. 5. This figure shows that the secondary irregularities have a helical configuration surrounding the billow cores. As time progresses, tracer mixing associated with the secondary instabilities obscures the billow structure which becomes disorganized, diffuse, and harder to discern. Meeting the CFL condition becomes increasingly difficult after T=10 in practice, and we have not explored the very late stages of instability.

Note that relating the 50 min. simulation time depicted here to the 30 min. observed lifetime of the banded echoes is not straightforward as we do not know the moment in the instability chronology when echoes become detectable. The simulation furthermore

lacks ionospheric chemistry and transport and cannot be used to assess the mechanism that causes echoes to cease. This will be the subject of future work.

Summary

We have presented VHF coherent scatter radar imagery of plasma density irregularities in sporadic *E* layers at geomagnetic latitudes of about 54°, under the midlatitude ionospheric trough and at the extreme northerly range of latitudes where E_s layers are statitically prolific. Radar images show that the echoes come from elongated, banded structures separated by tens of kilometers and propagating predominately to the southwest. This behavior is similar to what has been observed for many years at lower middle latitudes.

Quasiperiodic echoes such as those considered here are sometimes atrributed to coupled *E*/*F* region plasma instabilities (e.g. *Cosgrove and Tsunoda* [2004]; *Tsunoda* [2006]). That QP echoes occur under the midlatitude trough argues that coupled instabilities cannot be uniquely responsible for the phenomena. Observations of QP echoes in the subauroral zone further support the point [*Hysell et al.*, 2018b].

There is extensive evidence that Kelvin-Helmholtz instabilities are a common feature in the MLT region since the region is characterized by large winds and associated large shears. There are other instabilities in the region, however, that can lead to significant neutral upwelling of the type required to produce coherent radar echoes. *Larsen et al.* **[2004] and** *Hurd et al.* **[2009] pointed out the similarities between conditions in the atmospheric boundary layer and the MLT region, including strong rotational shears, wind profile inflection points, and a region of higher static stability overlying a region of lower static stability, which are all conditions required for convective roll, i.e., an Ekman-type, instability to form. More recently,** *Chkhetiani and Shalimov* **[2013] have suggested specifically**

that the convective rolls may be responsible for the frontal structures in sporadic *E* layers underlying the QP echoes. The Ekman instability theory predicts that the convective roll axes will be aligned at a horizontal angle between 10° and 20° relative to the wind direction. When observed from a fixed location, the overturning structures therefore appear to have a long period since the advective wind component perpendicular to the roll structure is small. Ground-based lidar observations show characteristic periods of 1 to 3 hours for the large-scale overturning in sodium layers. A more extensive discussion of the theoretical predictions and the observations can be found in the articles by *Larsen et al.* [2004] and *Hurd et al.* [2009]. Since the Ekman-type intability and associated overturning structures occur in the same altitude range as the strong sporadic *E* layers and coherent scatter structures, it is reasonable to expect that such instabilities can modulate the longer-term variation in the scattering layers when they are present, as suggested by *Chkhetiani and Shalimov* [2013]. Since the orientation of the convective rolls depends only on the wind direction at the height of the inflection point in the wind profile, the instability can account for observations of frontal structures propagating over a wide range of azimuth angles, something that the coupled plasma instability theory cannot.

Here, we have explored further another mechanism whereby neutral Kelvin Helmholtz instability is responsible for the E_s-layer structuring. Earlier studies based on radar observations in the Caribbean have shown that the wavelength, propagation speed, and propagation direction of the bands underlying the QP echoes are consistent with expectations for KH instabilities in the lower thermosphere where the neutral winds frequently meet the Richardson number criterion for instability.

In this paper, we have found that the primary QP-echo bands can be accompanied by secondary bands oriented nearly normally to the primaries with separation distances of a few km. Radar images of the secondary bands resemble the secondary KH instabilities found in 3D numerical simulations. Our surmise is that the nuetral flows surrounding the instabilities entrain the unmagnetized sporadic *E*-layer ions within them.

Once so structured, the *E*-layer plasma would become unstable to one of a number of possible gradient-type instabilities, ultimately producing the meter-scale irregularities from which the radar signals scatter. This last link in the causality chain has not been demonstrated theoretically or computationally and remains a subject for further study.

The observations analyzed here are somewhat reminiscent of the those of *Hecht et al.* [2021] who observed interactions between adjacent KH billow cores in airglow imagery of mesospheric OH layers. They observed secondary KH instabilities including convective instabilities near individual billows along with what appeared to be the "tubes" and "knots" identified by *Thorpe* [1985, 1987]. These features represent mergers between adjacent billow cores that are misaligned or otherwise deformed. *Fritts et al.* [2021] were able to recover these features in numerical simulations, arguing that they should occur wherever KH instabilities are modulated by forcing at larger scales due, for example, to gravity wave propagation. Their numerical simulation results resembled the radar images presented here in some respects. The authors concluded that secondary KH instabilities are widespread in the upper atmosphere and may be important factors in the overall transport and dissipation.

Acknowledgments. This paper uses ionospheric data from the USAF NEXION Digisonde network; the NEXION Program Manager is Annette Parsons. The GIRO ionosonde data resource is available through `https://hpde.io/SMWG/Observatory/GIRO`. The work was supported by NSF awards AGS-2011304 to Cornell University and AGS-2012994 to Clemson University. Data discussed in this paper can be accessed through the Cornell eCommons repository through https://doi.org/10.7298/8sxf-b977.

References

Bernhardt, P. A., The modulation of sporadic-E layers by Kelvin-Helmholtz billows in the neutral atmosphere, *J. Atmos. Sol. Terr. Phys.*, *64(12-14)*, 1487–1504, 2002.

Bourdillon, A., C. Haldoupis, and J. Delloue, High-frequency Doppler radar observations of magnetic aspect sensitive irregularities in the midlatitude *E* region ionosphere, *J. Geophys. Res.*, *100*, 21,503, 1995.

Burns, K. J., G. M. Vasil, J. S. Oishi, D. Lecoanet, and B. P. Brown, Dedalus: A flexible framework for numerical simulations with spectral methods, *Phys. Rev. Res.*, pp. 1–39, 2643–1564/2020/2(2)/023,068, 2020.

Chau, J. L., and R. F. Woodman, Low-latitude quasi-periodic echoes observed with the Piura VHF radar in the *E* region, *Geophys. Res. Lett.*, *26*, 2167, 1999.

Chau, J. L., J. M. Urco, V. Avsarkisov, J. P. Vierinen, R. Latteck, C. M. Hall, and M. Tsutsumi, Four-dimensional quantification of Kelvin-Helmholtz instabilities in the polar summer mesosphere using volumetric radar imaging, *Geophys. Res. Lett.*, *47*, https://doi.org/10.1029/2019GL086,081, 2020.

Chkhetiani, O. G., and S. L. Shalimov, Mechanism by which frontal structures in the ionospheric sporadic *E* layers are formed, *Geomagnetism and Aeronomy*, *53*, 177–187, 2013.

Chu, Y. H., and C. Y. Wang, Interferometry observations of 3-dimensional spatial structures of sporadic *E* using the Chung-Li VHF radar, *Radio Sci.*, *32(2)*, 817–832, 1997.

Corcos, G., and F. S. Sherman, Vorciticy concentration and the dynamics of the unstable free shear layer, *J. Fluid Mech.*, *73*, 241–264, 1976.

Cosgrove, R. B., Wavelength dependence of the linear growth rate of the *Es* layer instability, *Ann. Geophys.*, *25*, 1311–1322, 2007.

Cosgrove, R. B., and R. T. Tsunoda, A direction-dependent instability of sporadic- *E* layers in the nighttime midlatitude ionosphere, *Geophys. Res. Lett.*, *29(18)*, 1864, doi:10.1029/2002JA009,728, 2002.

Cosgrove, R. B., and R. T. Tsunoda, Instability of the *E–F* coupled nighttime midlatitude ionosphere, *J. Geophys. Res.*, *109*, doi:10.1029/2003JA010,243, 2004.

Ecklund, W. L., D. A. Carter, and B. B. Balsley, Gradient drift irregularities in mid-latitude sporadic *E*, *J. Geophys. Res.*, *86*, 858, 1981.

Fritts, D. C., S. A. Wieland, T. S. Lund, S. A. Thorpe, and J. H. Hecht, Kelvin-Helmholtz billow interactions and instabilities in the mesosphere over the Andes Lidar Observatory: 2. Modeling and interpretation, *J. Geophys. Res. Atmos.*, *126*, https://doi.org/10.1029/2020JD033,412, 2021.

Haldoupis, C., A. Bourdillon, M. Six, and J. Delloue, Midlatitude *E* region coherent backscatter observed simultaneously at two HF radar frequencies, *J. Geophys. Res.*, *101*, 7961, 1996.

Haldoupis, C., G. C. Hussey, A. Bourdillon, and J. Delloue, Aximuth-time-intensity striations of quasiperiodic radar echoes from the idlatitude E region ionosphere, *Geophys. Res. Lett.*, *28*, 1933–1936, 2001.

Hazel, P., Numerical studies of the stability of inviscid stratified shear flows, *J. Fluid Mech.*, *51(1)*, 39–61, 1972.

Hecht, J. H., D. C. Fritts, L. J. Gelinas, R. J. Rudy, R. L. Walterscheid, A. Z. Liu, and S. A. Thorpe, Kelvin-Helmholtz billow interactions and instabilities in the mesosphere over the Andes Lidar Observatory: 1. Observations, *J. Geophys. Res. Atmos.*, *119*, 9359 9375,doi:10.1002/2014JD021,833, 2021.

Hurd, L., M. F. Larsen, and A. Z. Liu, Overturning instability in the mesosphere and lower thermosphere: analysis of instability conditions in lidar data, *Ann. Geophys.*, *27*, 2937–2945, 2009.

Hysell, D. L., and J. Burcham, The 30 MHz radar interferometer studies of midlatitude *E* region irregularities, *J. Geophys. Res.*, *105*, 12,797, 2000.

Hysell, D. L., and J. L. Chau, Optimal aperture synthesis radar imaging, *Radio Sci.*, *41*, 10.1029/2005RS003,383, RS2003, 2006.

Hysell, D. L., M. Yamamoto, and S. Fukao, Imaging radar observations and theory of type I and type II quasi-periodic echoes, *J. Geophys. Res.*, *107 (A11)*, 1360, 2002.

Hysell, D. L., M. F. Larsen, and Q. H. Zhou, Common volume coherent and incoherent scatter radar observations of mid-latitude sporadic *E*-layers and QP echoes, *Ann. Geophys.*, *22*, 3277–3290, 2004.

Hysell, D. L., E. Nossa, M. F. Larsen, J. Munro, M. P. Sulzer, N. Aponte, and S. A. González, Sporadic *E* layer observations over Arecibo using coherent and incoherent scatter radar: Assessing dynamic stability in the lower thermosphere, *J. Geophys. Res.*, *114, A12303*, doi:10.1029/2009JA014,403, 2009.

Hysell, D. L., T. Yokoyama, E. Nossa, R. B. Hedden, M. F. Larsen, J. Munro, S. Smith, M. P. Sulzer, and S. A. González, Radar and optical observations of irregular midlatitude sporadic *E* layers beneath MSTIDs, in *IAGA Special Sopron Book Series, Aeronomy of the Earth's*

Atmosphere and Ionosphere, edited by B. Hultqvist, M. A. Abdu, D. Pacheva, and A. Bhattacharyya, Springer publisher, 2010.

Hysell, D. L., E. Nossa, M. F. Larsen, J. Munro, S. Smith, M. P. Sulzer, and S. A. González, Dynamic instability in the lower thermosphere inferred from irregular sporadic layers, *J. Geophys. Res.*, *117, A8*, doi:10.1029/2012JA017,910, 2012.

Hysell, D. L., E. Nossa, H. C. Aveiro, M. F. Larsen, J. Munro, M. P. Sulzer, and S. A. González, Fine structure in midlatitude sporadic *E* layers, *J. Atmos. Sol. Terr. Phys.*, *103*, 16–23, DOI: 10.1016/j.jastp.2012.12.005, 2013.

Hysell, D. L., M. F. Larsen, D. C. Fritts, B. Laughman, and M. P. Sulzer, Major upwelling and overturning in the mid-latitude F region ionosphere, *Nature Comm.*, *9*, 10.1038/s41,467–018–05,809–x, 2018a.

Hysell, D. L., J. Munk, and M. McCarrick, VHF radar images of artificial field-aligned ionospheric irregularities in the subauroral *E* region, *Radio Sci.*, *53*, 334–343, https://doi.org/10.1002/2017RS006,497, 2018b.

Klaassen, G. P., and W. R. Peltier, The onset of turbulence in finite amplitude Kelvin-Helmholtz billows, *J. Fluid Mech.*, *155*, 1–35, 1985.

Larsen, M. F., A shear instability seeding mechanism for quasi-periodic radar echoes, *J. Geophys. Res.*, *105(A11)*, 24,931–24,940, 2000.

Larsen, M. F., Winds and shears in the mesosphere and lower thermosphere: Results from four decades of chemical release wind measurements, *J. Geophys. Res.*, *107(A8)*, 1216, doi:10.1029/2001JA000,218, 2002.

Larsen, M. F., A. Z. Liu, C. S. Gardner, M. C. Kelley, S. Collins, J. .Friedman, and J. H. Hecht, Observations of overturning in the upper mesosphere and lower thermosphere, *J. Geophys.*

Res., *109, D02S04*, 10.1029/2002JD003,067, 2004.

Larsen, M. F., D. L. Hysell, Q. H. Zhou, S. M. Smith, J. Friedman, and R. L. Bishop, Imaging coherent scatter radar, incoherent scatter radar, and optical observations of quasiperiodic structures associated with sporadic *E* layers, *J. Geophys. Res.*, *112, A06321*, doi:10.1029/2006JA012,051, 2007.

Liu, H.-L., Large wind shears and their implications for diffusion in regions with enhanced static stability: The mesopause and the tropopause., *J. Geophys. Res. Atmos.*, *122*, 9579–9590, https://doi.org/10.1002/2017JD026,748, 2017.

Martinez, D. M. V., E. B. C. Schettini, and J. H. Silvestrini, Secondary Kelvin-Helmholtz instability in a 3D stably stratified temporal mixing layer by direct numerical simulation, *Mecánica Computational*, *25*, 217–229, 2006.

Mashayek, A., and W. R. Peltier, The 'zoo' of secondary instabilities precursory to stratified shear flow transition. Part 2 Effects of stratification, *J. Fluid Mech.*, *708*, 45–70, 2012.

Mesquita, R. L. A., M. F. Larsen, I. Azeem, M. H. Stevens, B. P. Williams, and R. L. Collins, In situ observations of neutral shear instability in the statically stable high-latitude mesosphere and lower thermosphere during quiet geomagnetic conditions, *Geophys. Res. Lett.*, *125*, https://doi.org/10.1029/2020JA027,972, 2020.

Miller, K. L., and L. G. Smith, Incoherent scatter radar observations of irregular structure in mid-latitude sporadic *E* layers, *J. Geophys. Res.*, *83*, 3761, 1978.

Perkins, F., Spread *F* and ionospheric currents, *J. Geophys. Res.*, *78*, 218, 1973.

Rao, N. V., A. K. Patra, and S. V. B. Rao, Some new aspects of low-latitude *E*-region QP echoes revealed by Gadanki radar: Are they due to Kelvin-Helmholtz instability or gravity waves?, *J. Geophys. Res.*, *113*, doi:10.1029/2007JA012,574, 2008.

Reinisch, B. W., and I. A. Galkin, Global ionospheric radio observatory (GIRO), *Earth, Planets, and Space*, *63*, 377–381, doi:10.5047/eps.2011.03.001, 2011.

Riggin, D., W. E. Swartz, J. Providakes, and D. T. Farley, Radar studies of long-wavelength waves associated with mid-latitude sporadic *E* layers, *J. Geophys. Res.*, *91*, 8011, 1986.

Schlegel, K., and C. Haldoupis, Observation of the modified two-stream instability in the mid-latitude *E* region, *J. Geophys. Res.*, *99*, 6219, 1994.

Seyler, C. E., J. M. Rosado-Roman, and D. T. Farley, A nonlocal theory of the gradient-drift instability in ionospheric plasmas at mid-latitudes, *J. Atmos. Sol. Terr. Phys.*, *66(17)*, 1627–1637, 2004.

Sherman, J. P., and C. Y. She, Seasonal variation of mesopause region wind shears, convective and dynamic instabilities above Fort Collins, CO: A statistical study, *J. Atmos. Sol. Terr. Phys.*, *68*, 1061–1074, 2006.

Smyth, W. D., Dissipation range geometry and scalar spectra in sheared, stratified turbulence, *J. Fluid Mech.*, *401*, 209–242, 1999.

Thorpe, S. A., Laboratory observations of secondary structures in Kelvin-Helmholtz billows and consequences for ocean mixing, *Geophys. Astrophys. Fluid Dyn.*, *34*, 175–199, 1985.

Thorpe, S. A., Transitional phenomena and the deelopment of turbulence in stratified fluids: a review, *J. Geophys. Res.*, *92*, 5231–5248, 1987.

Thorpe, S. A., On the Kelvin-Helmholtz route to turbulence, *J. Fluid Mech.*, pp. 1–4, 2012.

Tsunoda, R. T., On the coupling of layer instabilities in the nighttime midlatitude ionosphere, *J. Geophys. Res.*, *111, A11304*, doi:10.1029/2006JA011,630, 2006.

Tsunoda, R. T., S. Fukao, M. Yamamoto, and T. Hamasaki, First 24.5 MHz radar measurements of quasiperiodic backscatter from field-aligned irregularities in midlatitude sporadic *E*, *Geophys. Res. Lett.*, *25*, 1765, 1998.

Yamamoto, M., S. Fukao, R. F. Woodman, T. Ogawa, T. Tsuda, and K. Kato, Mid-latitude *E* region field-aligned irregularities observed with the MU radar, *J. Geophys. Res.*, *96*, 15,943, 1991.

Yamamoto, M., S. Fukao, T. Ogawa, T. Tsuda, and S. Kato, A morphological study of mid-latitude *E*-region field-aligned irregularities observed with the MU radar, *J. Atmos. Terr. Phys.*, *54*, 769, 1992.

Yamamoto, M., N. Komoda, S. Fukao, R. T. Tsunoda, and T. Ogawa, Spatial structure of the *E* region field-aligned irregularities revealed by the MU radar, *Radio Sci.*, *29*, 337, 1994.

Yang, N., H. Le, and L. Liu, Statistical analysis of ionospheric midlatitude trough over the Northern Hemisphere derived from GPS total electron content data, *Earth, Planets, and Space*, *67*, https://doi.org/10.1186/s40,623–015–0365–1, 2015.

Yu, B., X. Xue, X. Yue, C. Yang, C. Yu, X. Dou, B. Ning, and L. Hu, The global climatology of the intensity of the ionospheric sporadic *E* layer, *Atmos. Chem. Phys.*, *19*, 4139–4151, https://doi.org/10.5194/acp–19–4139–2019, 2019.

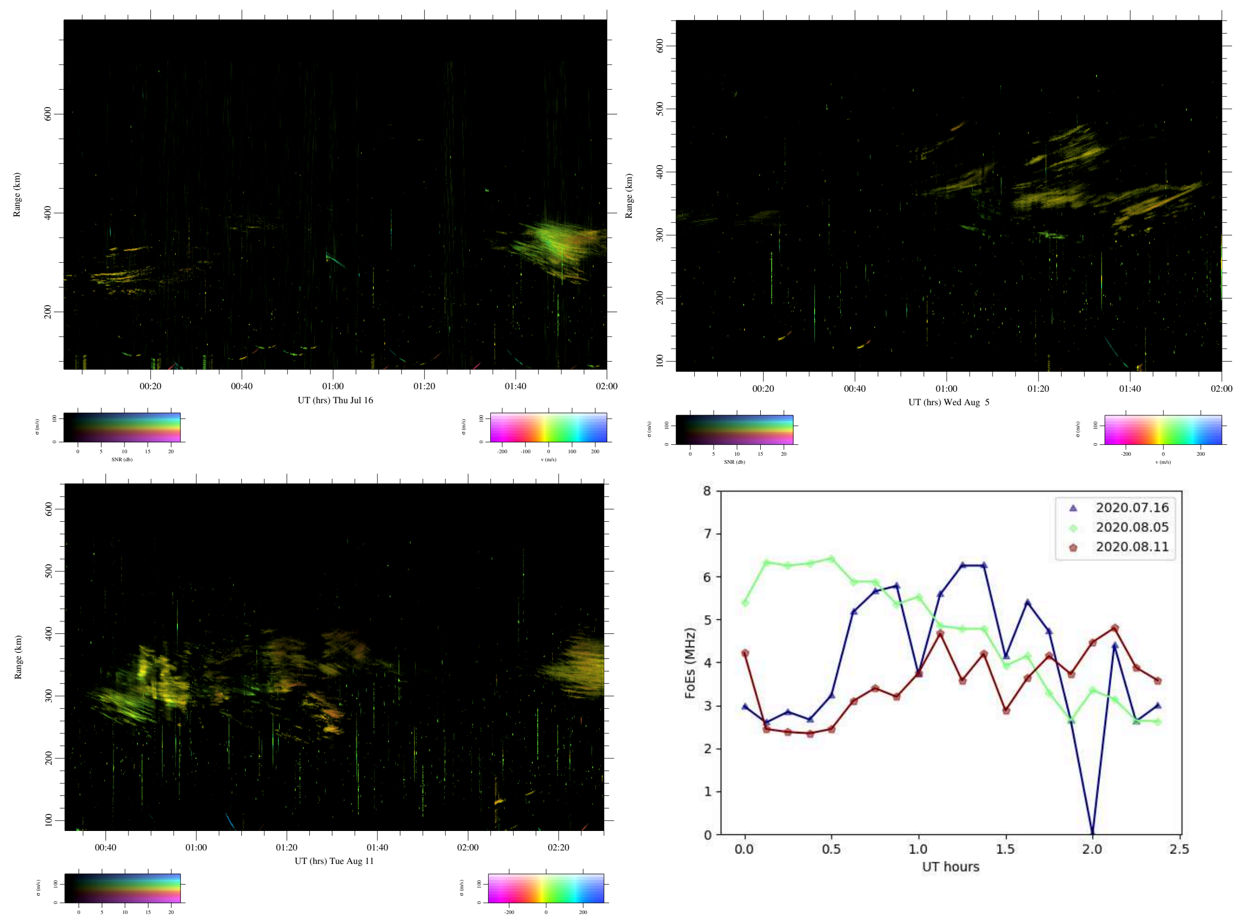

Figure 1. Range-time-Doppler-intensity (RTDI) plots for July 16, August 5, and August 11, 2020 (UT dates). The brightness, hue, and saturation of the pixels indicate the signal-to-noise ratio, Doppler shift, and spectral width of the backscatter according to the legends shown. The IPP was 750 km on July 16 and 600 km thereafter. Echoes from E_s-layer irregularities are range aliased, and their true range is the apparent range shown plus the IPP. Note that UT = EST + 5 = EDT + 4. The panel in the lower-right corner shows FoEs measured by the Alpena Digisonde for the three nights in question.

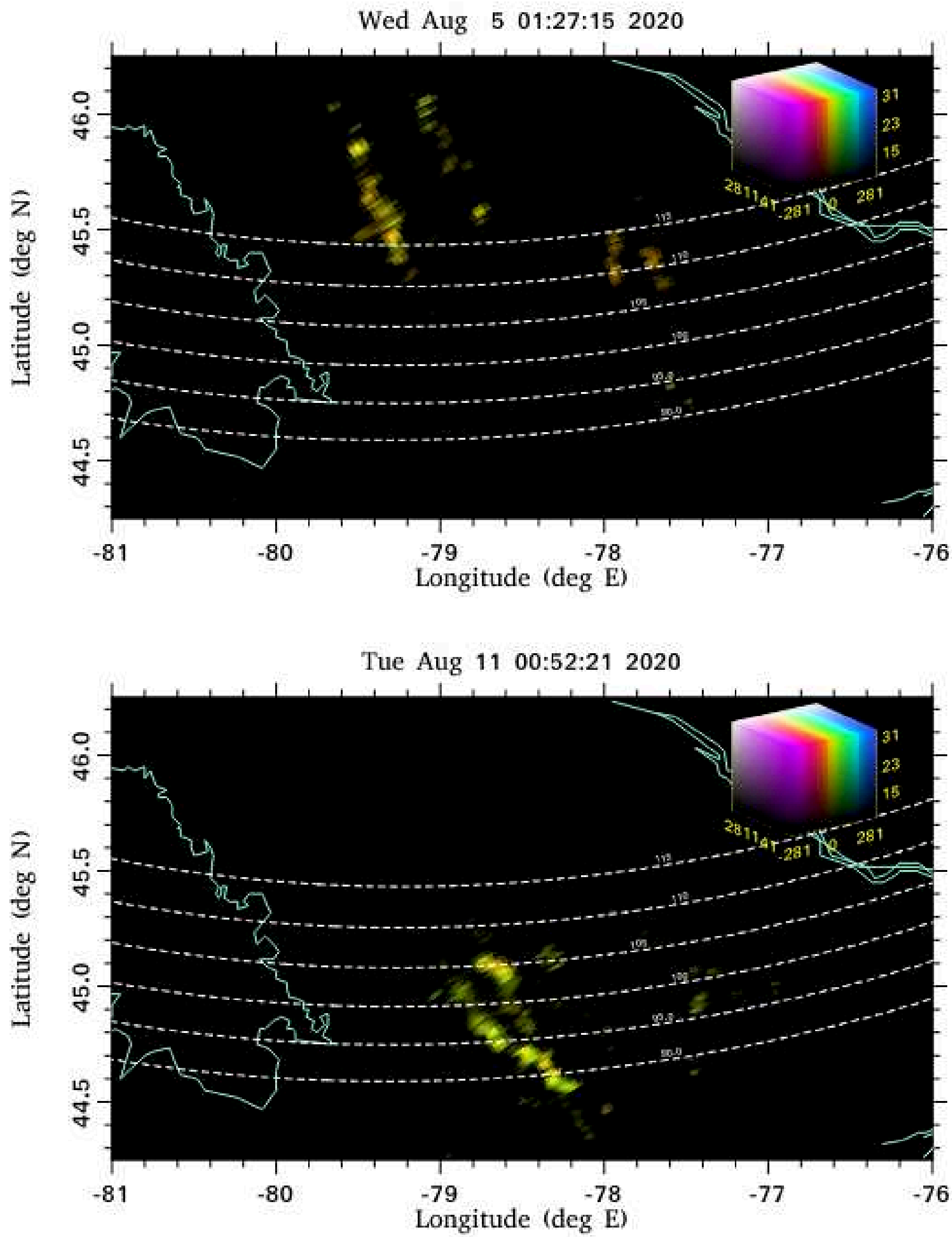

Figure 2. Radar images for August 5 (above) and August 11 (below), 2020, at the UT times indicated. The incoherent integration times for the images was 3 s. The color scales for the pixels in the images is the same as in the RTDI plots described above. White dashed contours are the loci of perpendicularity for various altitudes assuming straight-line propagation. The main features in both images are long banded structures which can be seen over time to propagate to the southwest.

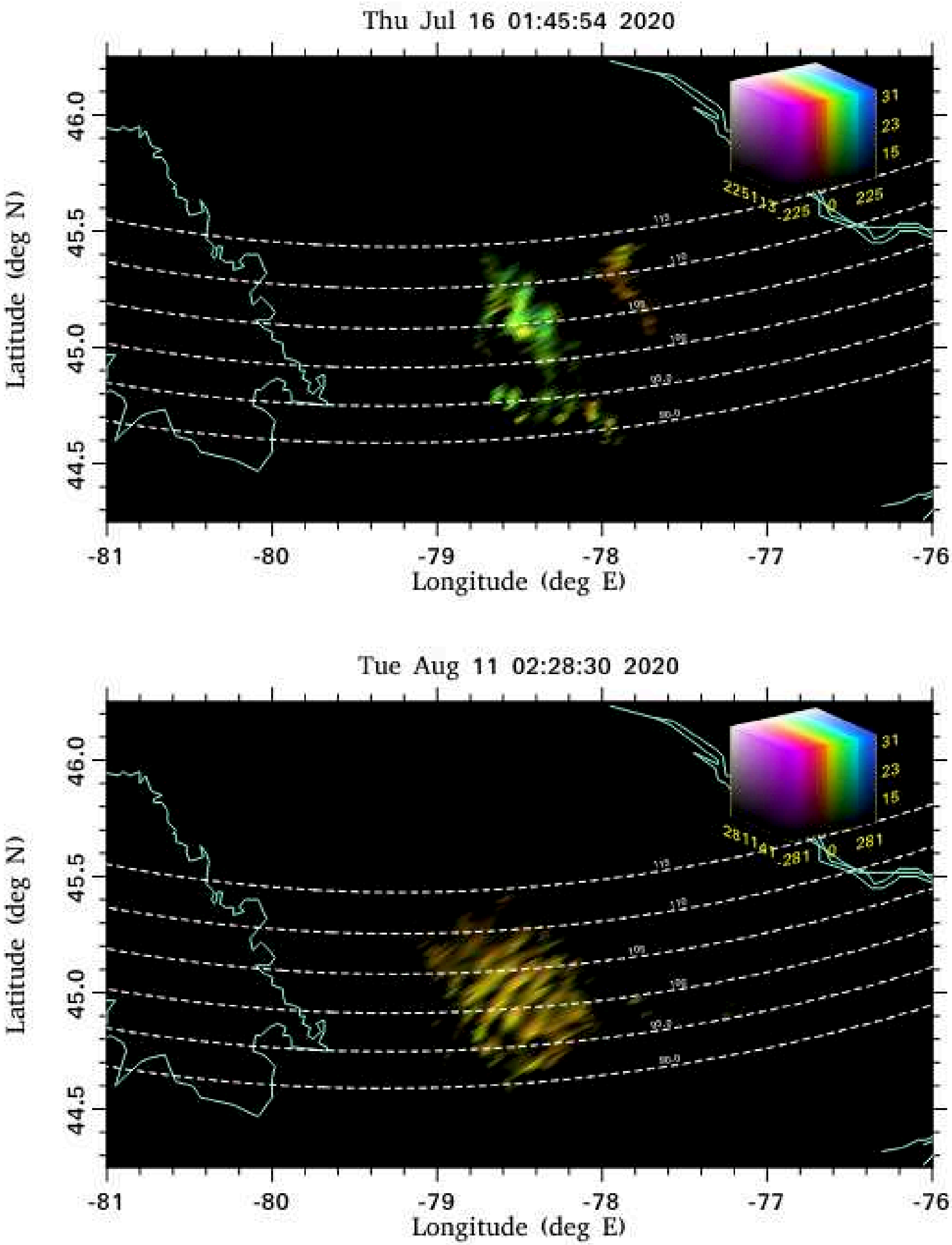

Figure 3. Same as in the previous figure except for July 16 and Aug. 11, 2020. The main features this time are broadened bands with transverse braided structure.

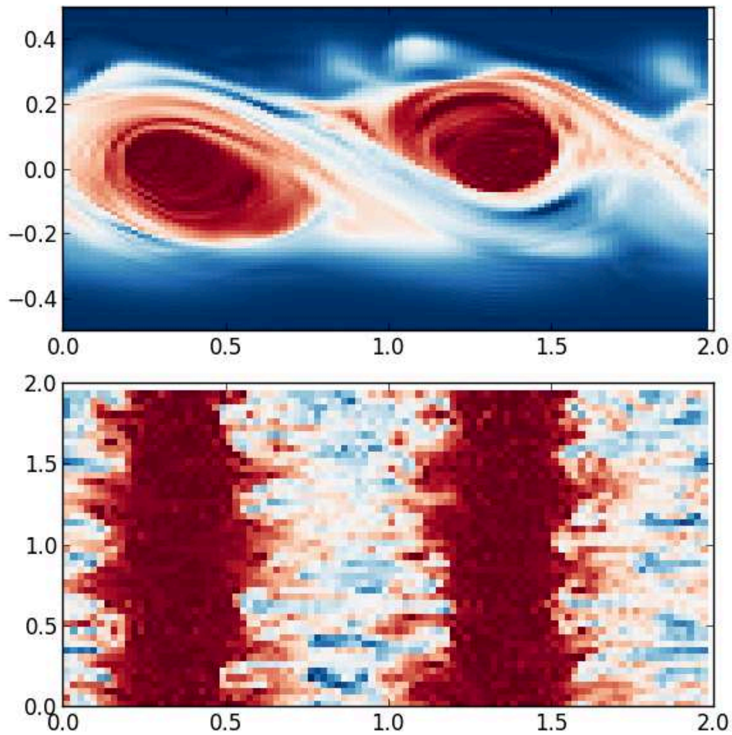

Figure 4. Numerical results at simulation time T=10. The horizontal axes of both panels represent the streamwise direction. The vertical axis of the top panel is the vertical direction, and the vertical axis of the bottom panel is the spanwise direction. The color scale represents the quantity ρ which is regarded as a tracer of the flow. Secondary instability and structuring in the billow cores in the spanwise direction is evident.

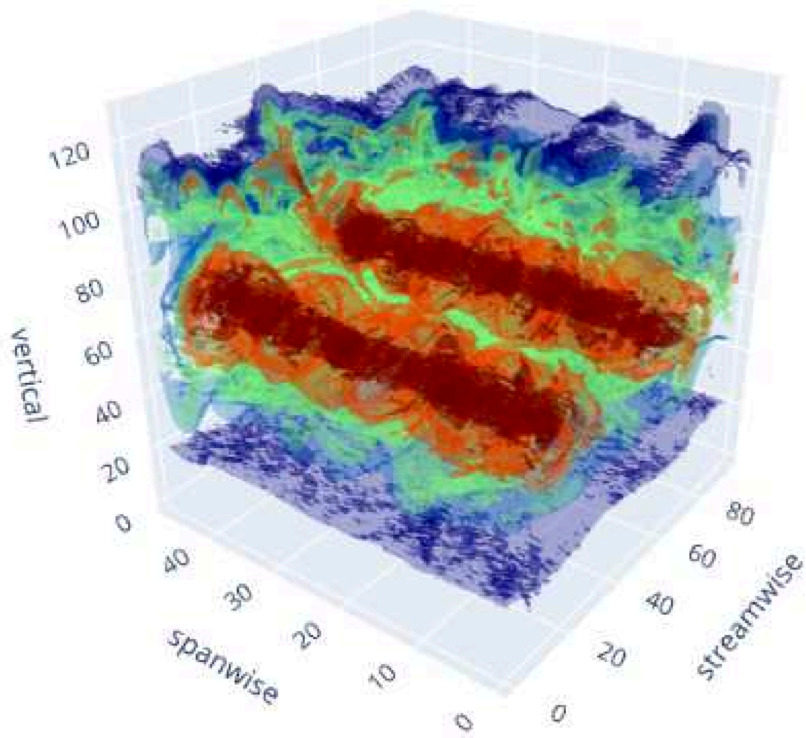

Figure 5. Same as in Fig. 4 except in three dimensions. Axis indices represent grid points. Here, the secondary structuring around the billow cores appears to be helical.